Photochemical fabrication of SnO_2 dense layers on reduced graphene oxide sheets for application in photocatalytic degradation of *p*-Nitrophenol

Ying Chen[a], Fengqiang Sun[a,b,c,*], Zhijian Huang[a], He Chen[a], Zefeng Zhuang[a], Zizhao Pan[a], Jinfeng Long[a], Fenglong Gu[a,b]

[a] School of Chemistry and Environment, South China Normal University, Guangzhou 510006, PR China
[b] Key Laboratory of Theoretical Chemistry of Environment, Ministry of Education, South China Normal University, PR China
[c] Guangzhou Key Laboratory of Materials for Energy Conversion and Storage, PR China

ARTICLE INFO

ABSTRACT

A room-temperature photochemical method was introduced to fabricate SnO_2-reduced graphene oxide (SnO_2-rGO) composite with a new type of structure. SnO_2 dense layers were directly grown on the two sides of an rGO sheet through ultraviolet light (UV) irradiation of a mixed precursor solution of $SnSO_4$, H_2SO_4, and graphene oxide for 6 h. The composite possessed a novel flat flake-like structure consisting of two SnO_2 dense layers and an rGO sheet sandwiched in between. In contrast to most graphene-based composites, the fabricated composite was non-flexible, wrinkle-free and rGO surfaces were completely covered. The composite could be used in photocatalysis and exhibited remarkably enhanced activity in degradation of *p*-nitrophenol under low intensity of UV light or sunlight. The activity was more than 12 times that of pure SnO_2 and considerably higher than that of other SnO_2-rGO composites. The dense layer immobilized the flat structure, promoted the photocatalytic activity, and maintained the long-term stability of the composite. After preservation of more than 12 months in ambient condition, the composite showed a nearly constant activity. This photochemical method can be used to fabricate graphene-based composites with regular structure, high performance, and long-term stability.

© 2017 Elsevier B.V. All rights reserved.

1. Introduction

Tin dioxide (SnO_2), an n-type semiconductor with a band gap of $\sim$3.57 eV, has attracted great interest in the fields of gas-sensor [1,2], lithium rechargeable battery [3], sensitized solar cells [4], and photocatalysis [5–8] because of its excellent electronic and optical properties and super stability. SnO_2 can be modified with other semiconductors [9–11], noble metals [12,13], or doped elements [14,15] to improve the electron-hole separation efficiency for efficient photocatalysis. Combining SnO_2 with graphene materials has become a new trend considering improved understanding of the properties of graphene materials [16–18].

Graphene, a single layer of sp^2–bonded carbon atoms, has been making a profound impact in many areas of science and technology ever since its discovery [19]. Graphene can be used as a

photocatalyst support material because of its unique properties, such as excellent electrical conductivity, high theoretical specific surface area, exceptional transparency, and adsorption activity [20]. Graphene oxide (GO), a derivative of graphene, is used as starting material for easy and efficient construction of graphene-based composites; GO is further changed into reduced graphene oxide (rGO) after combining with the target materials. In addition to many semiconductor–rGO composite photocatalysts [21–24], various SnO_2–rGO composites have been fabricated to enhance the photocatalytic activity of SnO_2 through chemical bath method [25], hydrothermal method [26], and solid-state chemical method [27]. For most composites, the surface of the rGO sheet is generally covered with discrete semiconductor nanoparticles and a large proportion of the surface is exposed. The composite exhibits high flexibility and contains many wrinkles induced by the flexible rGO sheets. A composite with a regular morphology is difficult to obtain. Moreover, such composite sheets, like soft cloth, are easy to stack and aggregate, resulting in the decrease of active sites. Although changing the morphology of a semiconductor (e.g., using nanorods with larger sizes instead of fine particles) or fabricating a specific

---

assembly of semiconductor and rGO sheets could reduce the aggregation and enhance the activity to a certain extent [28–31], the exposure of rGO surfaces was still difficult to prevent. The exposed rGO surfaces might adsorb some unpredictable molecules when the composites are used or preserved, resulting in negative effects on their activity and stability. In addition, the number of semiconductor particles on a single rGO sheet is too small, and many rGO sheets had to be used to meet the requirements of the photocatalytic activity of a composite. These disadvantages not only waste rGO, but also add chances of aggregations among composite units and the total exposed surface areas of rGO sheets. The fabrication of semiconductor dense layers that could completely cover the two sides of an rGO sheet and eliminate the flexibility of the corresponding composite is thereby necessary but still a challenge.

Herein, a new room-temperature photochemical method, which irradiates ultraviolet (UV) light to the GO sheet-dispersed surfactant-free solution of $SnSO_4$ and H_2SO_4, was introduced to prepare SnO_2 dense layers that completely cover the rGO sheets. Different from most semiconductor-rGO composites, the obtained composite unit was composed of two SnO_2 dense layers and an rGO sheet sandwiched in between. To distinguish the sheet-like structure of rGO or GO, the shape of the composite unit in this study was called "flake". The flake exhibited a fine non-flexible flat structure. The large area of close contacts between the SnO_2 layer and rGO sheet was beneficial to the separation of electron-hole when the composite was used in photocatalysis. The exposure of the rGO surfaces was avoided as much as possible, increasing the stability of the composite. To explain the photocatalytic activity of such composite, p-nitrophenol (PNP), one of the most hazardous refractory pollutants with high stability and solubility in water [32,33], was chosen as the target pollutant to be photodegraded. The composite exhibited 12 times higher activity than the pure SnO_2 particles because of its specific structure. Moreover, after exposure to ambient condition for more than 12 months, the composite still exhibited the nearly constant activity and had similar UV and solar photocatalytic activity. These observations demonstrate that the new SnO_2-rGO composite obtained by the photochemical method is promising and practical for environmental remediation applications.

2. Experimental details

2.1. Preparation of GO

GO was synthesized from graphite powder by modified Hummers' method [34]. Briefly, 3.0 g of powdered flake graphite and 1.5 g of $NaNO_3$ were added into 69 mL of concentrated H_2SO_4 into a flake cooled in an ice bath under agitation. Then 3.0 g of $KMnO_4$ was added to the suspension slowly maintaining the vigorous agitation at a temperature below 10 °C. The flask was taken out and placed into a water bath at a temperature of 35 °C. After 30 min, 90 mL of deionized water was slowly stirred into the paste to form a suspension. The suspension was stirred under 90 °C for 1 h and added with 100 mL of 3 vol.% H_2O_2 to reduce the residual $KMnO_4$ and MnO_2. When no bubbles were generated, the obtained suspension was washed by centrifugation with deionized water. The upper yellow grease was extracted and washed with water. The GO sheets were dispersed into deionized water to obtain a transparent and homogenous solution with concentration of 1.0 g L^{-1}.

2.2. Preparation of SnO_2 dense layers on rGO sheets

Briefly, 4.02 g of $SnSO_4$ was dissolved in 200 mL of 3 wt% H_2SO_4 solution in a beaker and added with 30 mL of 1.0 g L^{-1} GO solution to obtain the precursor solution. The existence of H_2SO_4 could lead to the formation of an acid surrounding in the solution, preventing the hydrolysis of Sn^{2+}. The solution was then ultrasonically treated for 30 min and added with deionized water to obtain a total volume of 300 mL. The solution was transferred into a Petri dish and placed on a magnetic stirrer under a UV tube-like lamp (Philips, 254 nm, 8 W) in a box. The solution was continuously stirred at 400 rpm. The lamp was turned on, and the light intensity on the surface of the solution was tuned to 0.86 mW/cm^2. Photochemical reactions occurred to induce the formation of SnO_2 dense layers on the GO sheets and the reduction of GO. After 6 h, the lamp and the stirrer were turned off successively. By centrifugation, all solids were collected and repeatedly washed with deionized water until the separated solution reached a neutral state. After drying at 60 °C for 12 h, SnO_2-rGO nanocomposites were finally obtained. The sample was named SR–6 h, according to UV light irradiation time in the fabrication process. The pure SnO_2 sample was prepared by the same process, except for the addition of GO sheets in the precursor solution.

2.3. Characterizations

The morphologies of the rGO-SnO_2 nanocomposites were directly investigated with scanning electron microscope (SEM, Shimadzu SS-550 and Quanta 250 FEG) and transmission electron microscope (TEM, JEOL JEM-2100HR). The compositions of the samples were characterized via X-ray powder diffraction (XRD, D/max2200, with Cu-Kα radiation), X-ray photoelectron spectrometry (XPS, ESCALAB 250 Xi), and Raman spectrometry (Nicolet NXR9650). The specific surface area (SSA) of a sample was measured by a Rapid BET Surface Area Analyzer (Type: Monosorb, Company: Quantachrome, America), using the rapid dynamic flow method.

2.4. Photocatalysis

The photocatalytic degradation of PNP was carried out in an aqueous solution under ambient conditions. Briefly, 0.05 g of catalyst was dispersed in 200 mL of 0.02 g L^{-1} PNP solution in a Petri dish. The solution was continuously stirred at 400 rpm during the photocatalytic reaction. The UV tube-like lamp (Philips, 254 nm, 8 W) was still chosen as the light source and placed above the dish. The light intensity near the surface of the solution was measured as 0.86 mW/cm^2. After the photocatalytic degradation started, 5 mL of the solution was obtained every 10 min from the Petri dish and centrifuged immediately to remove any suspended solids. The transparent solution was analyzed with a UV–vis spectrophotometer (UV-2500PC), and the absorbance was measured at a wavelength of 316 nm, corresponding to the maximum absorption wavelength of PNP. The total organic carbon (TOC) of the PNP solutions was analyzed with a Shimadzu TOC-VCPH analyzer to evaluate the mineralization degree of the organic material.

3. Results and discussion

3.1. Morphology and composition

Morphological and structural features of GO, SnO_2-rGO (SR–6 h), and pure SnO_2 were examined with SEM and TEM. Fig. 1A shows the SEM image of GO pristine sheets. The GO sheets are very thin, full of wrinkles, and edges are difficult to discern, which can also be reflected in the TEM image (Fig. 1B). The high resolution TEM image (HRTEM) of a GO sheet (inset of Fig. 1B) shows no lattice fringes, confirming the disordered nature of GO as described elsewhere [35]. Fig. 1C shows the SEM image of SR–6 h, which is composed of nanoflakes with a nearly flat structure, non-uniform plane sizes, and irregular edges. The flakes are non-flexible, wrinkle-free, and
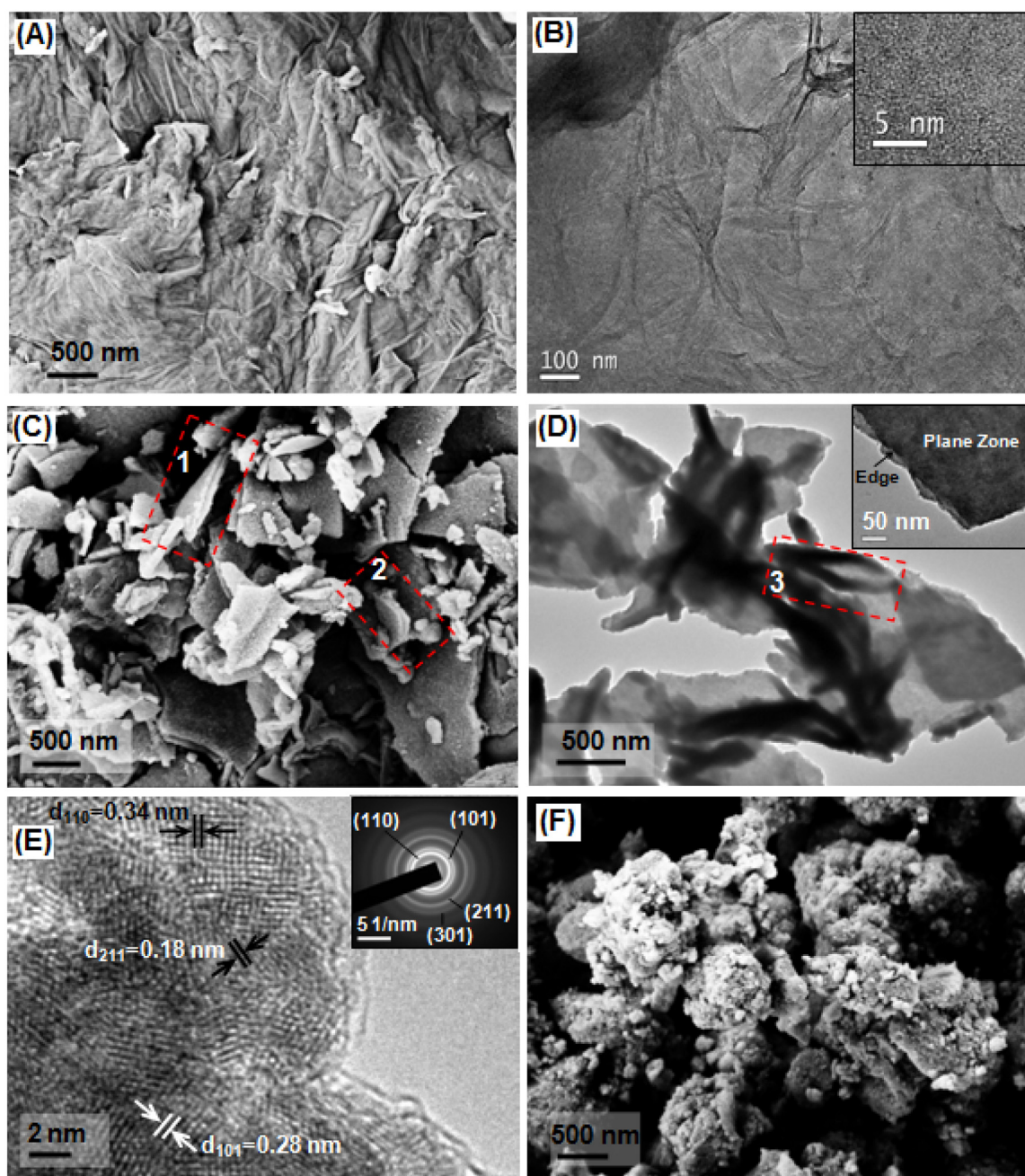
Fig. 1. Morphologies of GO, SR–6 h, and pure SnO$_2$. (A) SEM image of GO; (B) TEM and HRTEM image (the inset) of GO; (C), (D) and (E) SEM, TEM and HRTEM image of SR–6 h, respectively; (F) SEM image of the pure SnO$_2$.

nearly no aggregation or overlap exists among them, different from the pristine GO sheet and most graphene-based composite materials reported previously. A flake appears to be constituted of two dense layers bonded together, as shown in Zone 1 and Zone 2. The TEM image of this sample is shown in Fig. 1D. The uniform flat structure and the two dense layers (Zone 3) of a flake can be further recognized. The thickness of the flake is measured as ∼75 nm. An enlarged TEM image of a single flake (inset of Fig. 1D) shows the Plane Zone of the flake is uniformly dense and the edge displays a layered structure. Upon observation of the HRTEM (Fig. 1E), lattice fringes with distances of 0.34, 0.28, and 0.18 nm corresponding to the crystallographic planes (110), (101), and (211) of SnO$_2$, are found in nearly all the Plane Zone, explaining this side of the flake is composed of closely packed SnO$_2$ nanoparticles. The existence of grain boundaries and the selected area electron diffraction (SAED)

pattern (inset of Fig. 1E) of this sample display the polycrystalline characteristic of the SnO$_2$ dense layer. At the edge of the flake, under the SnO$_2$ layer, the rGO sheet with layered structures and without lattice fringes can be identified. Referring to Zones 1–3 of Figs. 1C and 1D, another SnO$_2$ dense layer could be inferred to adhere to the other side of the rGO sheet; the rGO sheet is sandwiched by two SnO$_2$ dense layers. Completely different from the morphology of SR–6 h, the pure SnO$_2$ sample is shown to consist of aggregated irregular particles (Fig. 1F).

Fig. 2A shows the X-ray diffraction (XRD) patterns of the above samples. The pattern of GO exhibits a sharp peak at 2θ = 9.5°, corresponding to a d-spacing of 1.03 nm, which is much larger than the d-spacing of natural graphite at 0.335 nm [36]. This change indicates that graphite is oxidized to form GO. The patterns of the SR–6 h and the pure SnO$_2$ samples are similar and show the characteristic
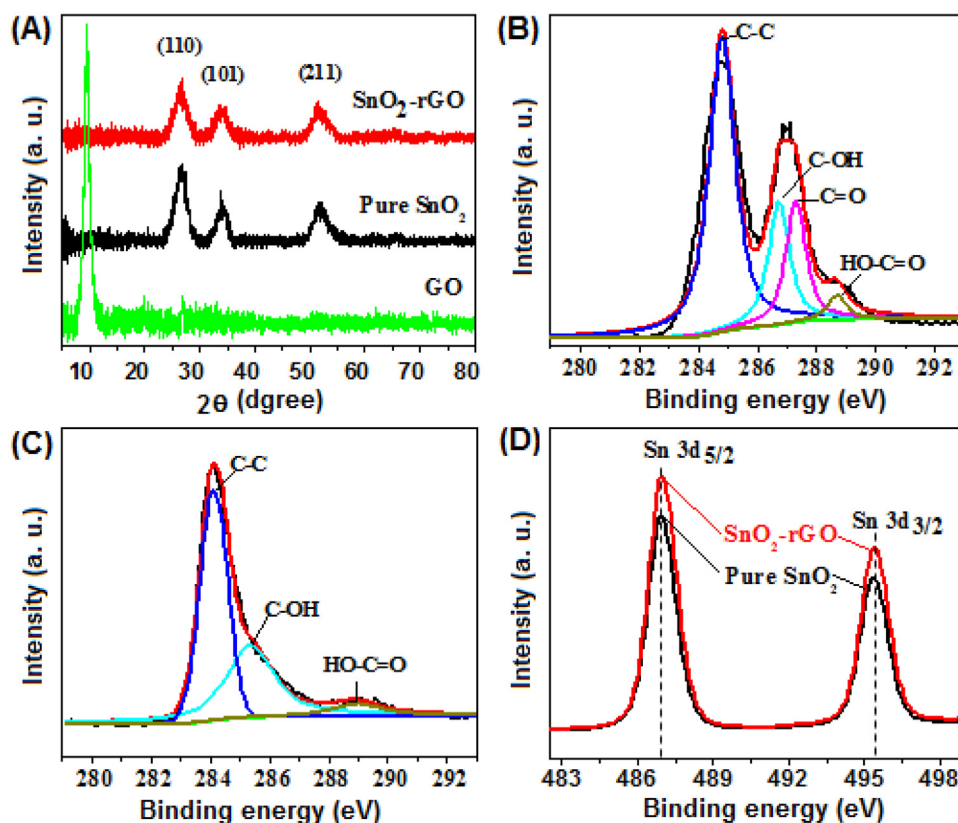
Fig. 2. Analysis on the composition of the GO, SR–6 h, and the pure SnO$_2$. (A) XRD spectra; (B) and (C) C 1 s XPS spectra of GO and SR–6 h, respectively; (D) Sn 3d spectra of the SR–6 h and the pure SnO$_2$.

peaks at 2θ values of 26.1°, 33.8°, and 51.5°, which correspond to the (110), (101), and (211) crystal faces of tetragonal SnO$_2$, respectively. The prominent diffraction peaks indicate that the SnO$_2$ generated under UV irradiation has good crystallinity. Notably, no separate peak is observed for rGO in SR–6 h, possibly because of the low loading content of rGO and low intensity of rGO [37]. Moreover, the characteristic peak (at ∼25°) of rGO may be screened by the main peak of SnO$_2$ [38]. XPS measurements of GO sheets and SR–6 h were carried out determining the existence state of carbon element. Fig. 2B shows the high-resolution and curve fit C 1 s XPS spectrum of the pristine GO sheets. Four peaks centered at 284.8, 286.8, 287.3, and 288.7 eV are observed corresponding to C—C, C—O, C=O, and OH—C=O groups, respectively [39]. By contrast, in the C 1 s spectrum of the SR–6 h (Fig. 2C), C=O groups had been removed and the quantity of C—O and OH—C=O groups were clearly decreased. This observation indicated that the GO incorporated in the composite had been reduced during the formation of SnO$_2$ under UV. The Sn core-level XPS spectrum of SR–6 h shows two peaks centered at 487.0 and 495.4 eV (Fig. 2D), which are respectively assigned to the Sn 3d$_{5/2}$ and Sn 3d$_{3/2}$ spin−orbital splitting photoelectrons in the Sn^{4+} state [40]. In comparison to the Sn 3d spectrum of the pure SnO$_2$, the peak positions are not changed, demonstrating no chemical bond between the SnO$_2$ and the rGO. The SnO$_2$ dense layer and the rGO sheet are combined by van der Waals force.

3.2. Growth mechanism

To reveal the growth mechanism of SnO$_2$ layers, SEM images (Fig. 3A–E) and SSAs (Fig. 3F) of the products from different irradiation times were observed and analyzed. Similar to naming of SR–6 h, samples from 0.5, 3.0, 12.0, and 24.0 h were also named as SR-0.5 h, SR-3 h, SR-12 h, and SR–24 h, respectively. For

SR-0.5 h (Fig. 3A), the composites retained the typical character of rGO sheet, i.e., stacking and wrinkling, because of short irradiation; an enlarged image of Zone 1 showed separated SnO$_2$ particles adhered to the rGO sheet. The sample had a SSA of 29.1 m^2/g, which is larger than that of the pure SnO$_2$ (9.5 m^2/g) but lower than that of the other samples (Fig. 3F). As the irradiation was increased to 3 h (Fig. 3B), SnO$_2$ particles combined into thin layers with a certain degree of mechanical strength. The wrinkle feature of the rGO sheets disappeared and SnO$_2$-rGO composite flat flakes began to appear. The surface of the SnO$_2$ layer displayed obvious porous structure (inset of Fig. 3B) and few aggregates, resulting in higher SSA (110.8 m^2/g) of SR–3 h than SR-0.5 h. However, the presence of the porous structure also indicates that the SnO$_2$ layer exhibits low densification degree, low mechanical strength, and minimal contact and adhesion to the rGO sheet. Some flakes might be seriously curved (as marked in Fig. 3B), leading to break down and exfoliation of partial SnO$_2$ layers during sample collection. The layer could be broken into small pieces and exfoliated as a whole, leaving partial rGO surface exposed. As shown in Fig. 3C and Fig. 1C–D, the SnO$_2$ layers became denser with increasing irradiation time up to 6 h; as such, no porous structure was identified (inset of Fig. 3C). As a result of the formation of the dense structure, the SnO$_2$ layers and their combinations with rGO sheets were further intensified, effectively immobilizing them on rGO sheets and suppressing the flexibility of rGO sheets. The composite flakes thereby displayed well flat structure with nearly no aggregation. The dense structure was detrimental, but the decreased aggregation promoted the increase in the specific surface area, leading to a relatively higher SSA (106.4 m^2/g), which is only a slightly lower than that of SR–3 h. However, continuously increasing the irradiation time to 12 and 24 h, some flakes grew (Fig. 3C) or stacked (Fig. 3D) together, and fewer individual flakes could be found. The cross-section of the
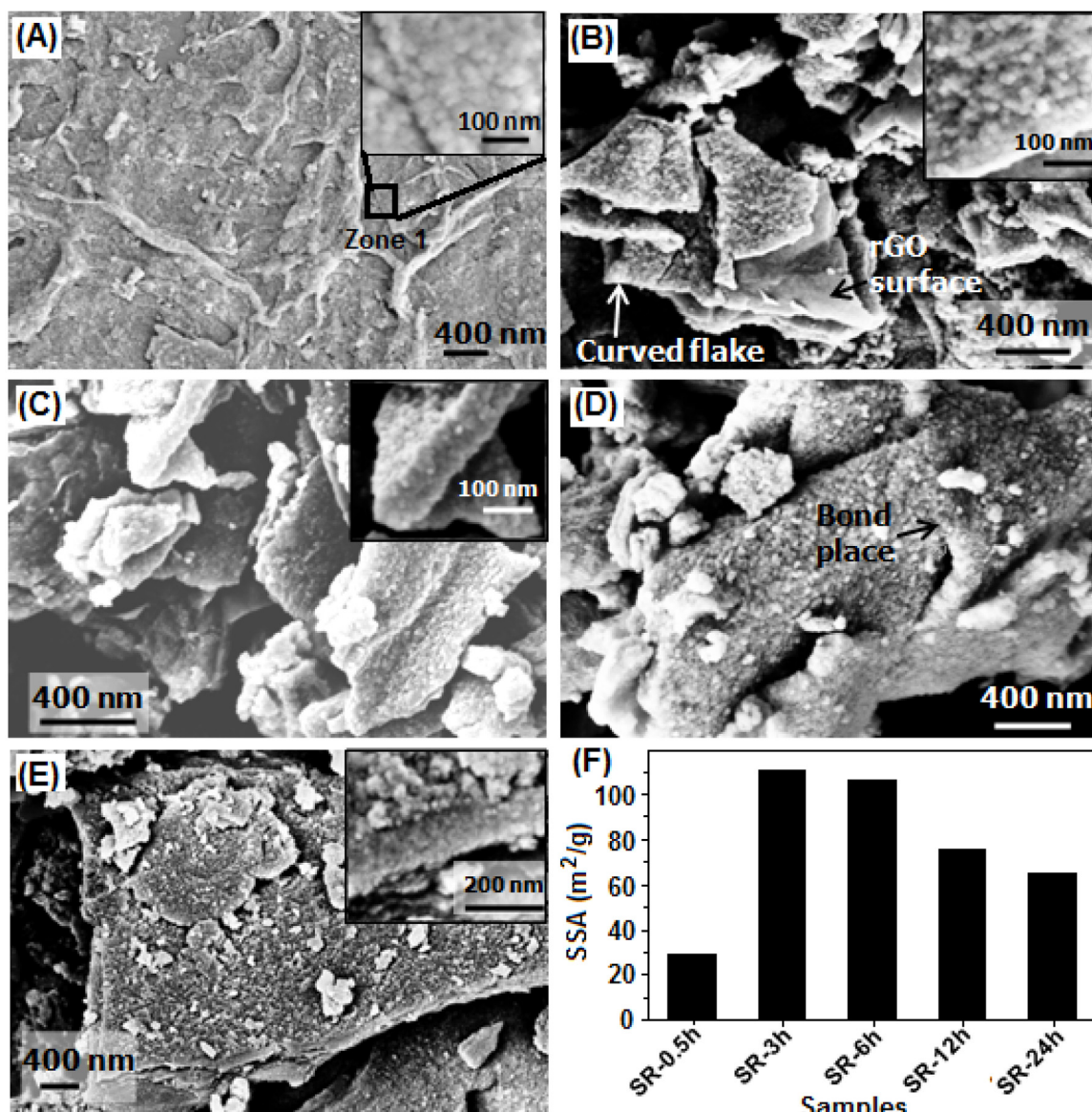
Fig. 3. SEM morphologies of SnO$_2$-rGO samples from UV irradiation time of 0.5 h (A), 3.0 h (B), 6.0 h (C), 12.0 h (D), and 24.0 h (E), and their SSAs (F).

SnO$_2$ layer displayed denser structure (inset of Fig. 3E). These samples exhibited decreased SSA (75.1 m^2/g for SR–12 h and 64.9 m^2/g for SR–24 h).

Raman spectra of the pristine GO sheets and the SnO$_2$-rGO composites at 3, 6, and 24 h were selectively measured, as shown in Fig. 4. On the curves from the composite, the bands peaking at ~631, ~703, ~779 and 996 cm^{-1} are all attributed to the characteristic peaks of SnO$_2$ [41,42]. The GO and the composites contain both G band (~1573 cm^{-1}, E$_{2g}$ phonon of sp^2 atoms) and D bands (~1340 cm^{-1}, κ-point phonons of A$_{1g}$ symmetry), further confirming that GO had been introduced. The intensity ratio of the D band to the G band (I$_D$/I$_G$) was calculated as 0.913 for GO, while this value was gradually increased to 0.925, 0.959, and 1.110 for the composite flakes at 3, 6, and 24 h irradiations, respectively. The increase in the intensity of D/G ratio indicates a decrease in the average size of the sp^2 domains formed during the photochemical reactions. This phenomenon can be allowed only when newly formed graphitic domains are smaller in size but greater in number compared with those present in GO before UV irradiation, as reported by Ruoff et al. [43], on the hydrothermal treatment of GO.
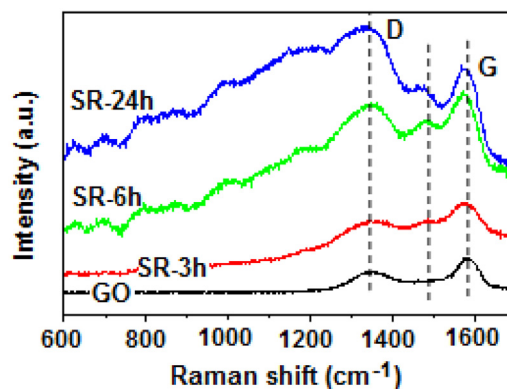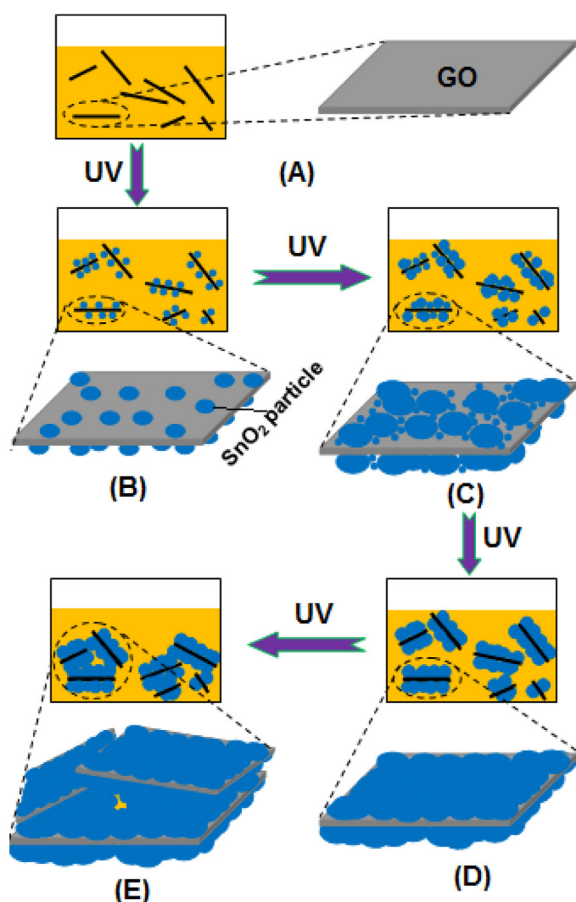

Fig. 4. Raman spectra of GO, SR–3 h, SR–6 h, and SR–24 h.

Based on this phenomenon and the XPS measurement of a SnO$_2$-rGO sample (Fig. 2C), the reduction degree of rGO can be confirmed gradually increased with increasing UV irradiation time [44,45]. In addition, with the increase of the irradiation time, the position of

Scheme 1. Formation process of SnO_2 dense layers on an rGO sheet under UV irradiation. (A) GO sheets in the precursor solution; (B) Nucleation of SnO_2 on the rGO sheet; (C) Growth of SnO_2 particles and forming of new nuclei; (D) Formation of dense layers on the rGO sheet; (E) Aggregation or stacking of SnO_2-rGO flakes because of prolonged irradiation time.

activity and could immediately react with the O_2 dissolved in the solution to be transformed into SnO_2 particles (Eq. (2)) (Scheme 1B). This process could be confirmed in a control experiment (see the supporting information) in which a product containing metallic Sn was obtained in the N_2 surrounding and the metallic Sn was easily oxidized into SnO_2 in air (Fig. S1). The two sides of a GO sheet are equal to induce the formation of SnO_2 particles. Notably, SnO_2 has a bandgap of around 3.57 eV and can be excited to generate electrons and holes by the UV light with a wavelength of 254 nm (Eq. (3)). Thus, during the formation of SnO_2 particles, electrons could also be gradually generated to reduce the GO into rGO (Eq. (4)), following the photocatalytic reduction process of GO reported elsewhere [37,50]. The SnO_2 particles continuously grew with increasing UV irradiation time. The new solid–solid interfaces between SnO_2 particles and rGO sheets or among adjacent SnO_2 particles are constituted and function as new nucleation sites to induce the repeated formation of new SnO_2 particles, filling all interstices (Scheme 1C). This step leads to the gradual densification of the SnO_2 layers until the formation of dense layers (Scheme 1D), which could be confirmed by Figs. 3A–E. This process also indicate that the chemical combinations among SnO_2 particles and the contacts between SnO_2 layers gradually increased, intensifying the SnO_2 layers and increasing the van der Waals force. The dense layers could immobilize the flat structure of the rGO sheet and the final composite, as shown in the SR–6 h sample. However, prolonged UV irradiation time would lead to too thick and too heavy composite flakes. The flakes thereby easily contacted each other and settled down to form aggregates or stacks (Scheme 1E and Figs. 3E–F). Obviously, suitable irradiation time is necessary for obtaining the SnO_2 dense layers and the flat flake-like structure of the composite. In this study, 6 h of irradiation was thereby optimized.

$$2Sn^{2+} + h\nu \rightarrow Sn \downarrow + Sn^{4+} \tag{1}$$

$$Sn + O_2 \rightarrow SnO_2 \tag{2}$$

$$SnO_2 + h\nu \rightarrow e^- + h^+ \tag{3}$$

$$GO + e^- + 2H^+ \rightarrow rGO + H_2O \tag{4}$$

3.3. Photocatalytic activity

The as-prepared flat composite flakes with dense SnO_2 layers (SR–6 h) could be used in photocatalytic degradation of pollutants in aqueous solution. For evaluating its activity, the photocatalytic degradation reactions of PNP in the presence of the pristine GO, the pure SnO_2 sample, and every obtained SnO_2-rGO composite under the same UV light source were observed and compared. Prior to photocatalytic experiment, the PNP solution with a catalyst was kept in the dark to attain the absorption−desorption equilibrium of the PNP with the catalyst. Every sample nearly had no adsorption for PNP. Fig. 5A displays the photodegradation efficiencies of PNP with different catalysts in 90 min of light exposure. In the presence of GO, the concentration of PNP was nearly constant, indicating that GO had no activity. The pure SnO_2 powder could play as a photocatalyst to degrade PNP, but because of its lower activity, only 19.3% PNP was decomposed; SR-0.5 h sample had similar effects. However, in the presence of any other SnO_2-rGO sample, the photodegradation was remarkably enhanced, although there were still differences because of the different activities of the catalysts. The flat composite flakes (SR–6 h) obviously had the highest activity and could lead to 95.6% PNP degradation, whereas samples SR–3 h, SR–12 h, and SR–24 h only led to 57.7%, 80.3%, and 79.2% degradation, respectively. The photodegradation reaction of PNP with any catalyst agrees well with pseudo-first-order kinetics (Fig. 5B). An integrated rate equation is suggested as follows: $\ln(C_0/C_t) = kt$ [51], where C_0 and C_t are the initial concentration and concentration at time t of PNP, and k is the apparent reaction rate (ARR) constant.

G peak gradually red shifted from ∼1581 cm^{-1} of pristine GO to ∼1567 cm^{-1} of SnO_2-rGO sample from 24 h irradiation, and a weak peak gradually appeared between D and G peaks. These observations could be attributed to the split of G peak caused by the generated tension of rGO sheets, as reported by Tang et al. [46], about the effect of SiO_2 layer on the G peak of rGO. Furthermore, the attached SnO_2 layers introduced a tensile stress on the rGO sheet through the van der Waals force, and the tensile stress was enhanced with the increase of the densification degree of the SnO_2 layers. The regular variation of the G peak obviously reflected the gradual densification process of SnO_2 layers with the increase of the UV irradiation time.

Based on the above analyses, the formation of the SnO_2 dense layers on an rGO sheet is described in the following process. The pristine GO sheets combined with many hydrophilic oxygen-containing groups can be well dispersed in water. The surface of GO sheets is negatively charged because of ionization of carboxyl groups (−COOH) [47], thereby preventing aggregation and promoting the maintenance of the flat structure of the sheets (Scheme 1A). After mixing the GO solution with $SnSO_4$ and H_2SO_4 solution, Sn^{2+} ions would be concentrated on the surfaces of GO sheets because of the electrostatic adsorptions. Under the UV irradiation, Sn^{2+} ions adsorbed the photons to generate metallic Sn and Sn^{4+} ions (Eq. (1)) [48,49]. The metallic Sn nuclei preferentially formed and grew on the surface of GO sheets, because the hydrophilic solid surface possessed a lower nucleation barrier than other parts of the solution. The newly-formed metallic Sn nuclei or nanoparticles had high
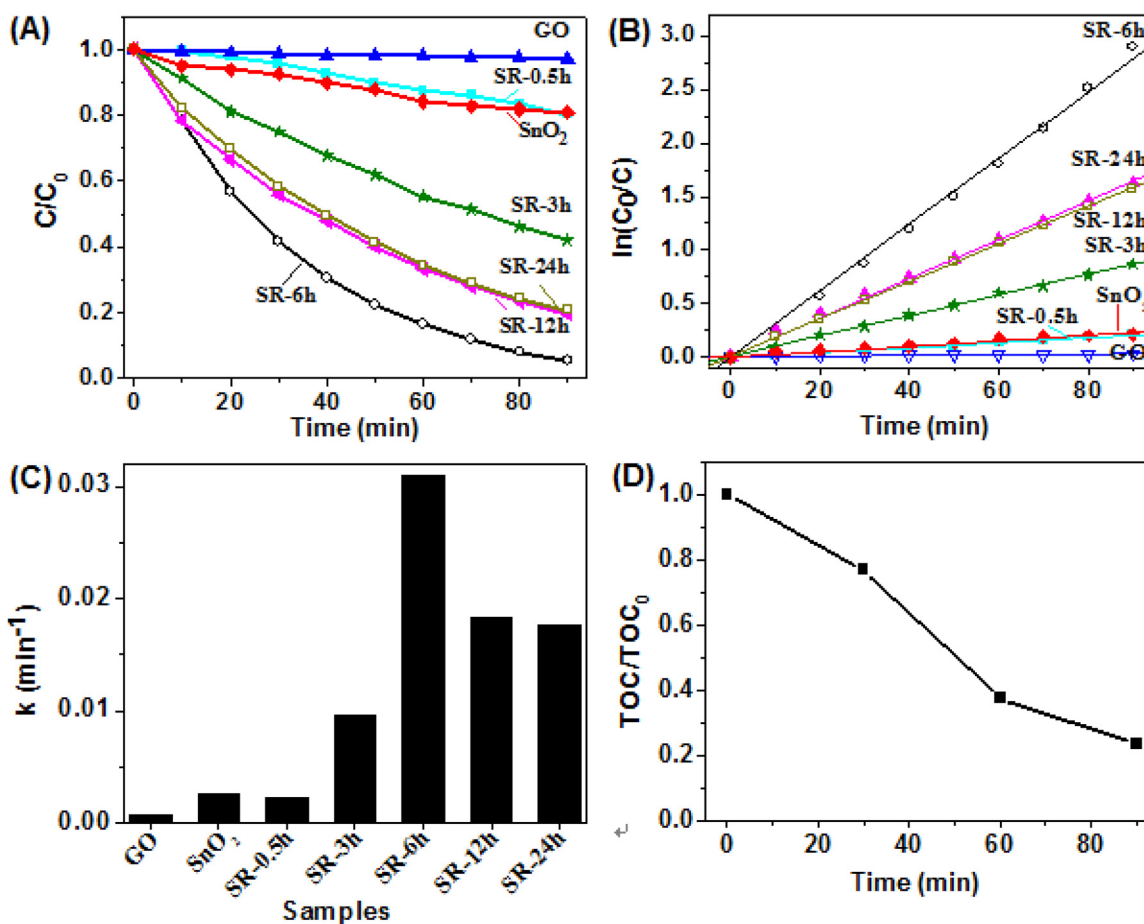
Fig. 5. Photocatalytic performances of SR–6 h and other catalysts in PNP photodegradation. (A) Degradation dynamics at 120 min; (B) First order kinetic simulations of different degradation processes; (C) Summary of the apparent reaction rate constants; (D) Changes of TOC during the degradation in the presence of SR–6 h.

The ARR constants of all degradation reactions are summarized in Fig. 5C, which intuitively reflects the activities of catalysts. The pure SnO_2 presented a lower ARR constant of 0.0026 min^{-1}. SnO_2-rGO composites presented regularly changed ARR constants with fabrication time (i. e., the UV irradiation time in the fabrication process of a product). The ARR constants gradually increased with increasing fabrication time within 0.5–6 h, exhibited an opposite change trend within 6–24 h. Nevertheless, the constants of SR-12 and SR-24 were similar. The SR–6 h sample presented the highest ARR constant of 0.0318 min^{-1}, which is more than 12 times than that of the pure SnO_2 and is considerably higher than those of other composites. To evaluate the effect of SR–6 h on the mineralization of PNP, the total organic content (TOC) of the PNP solution during its photodegradation was analyzed (Fig. 5D). The TOC gradually decreased, and the maximum TOC removal of PNP reached 76.3% after 90 min when no PNP molecule was detected. This finding confirmed the progressive mineralization of PNP caused by rapid and efficient decomposition of aromatic intermediates.

3.4. Photocatalytic mechanism

Generally, the photocatalytic oxidization of a pollutant in an aqueous solution follows a hole (h^+), superoxide radical ($•O_2^-$), hydroxyl radical ($•OH$), or mixed oxidization pathway decided by the catalyst and the pollutant. Holes naturally generated accompanying the generation of photogenerated electrons (e. g. Eq. (3)); superoxide radicals generated from the reaction of electrons with the dissolved O_2 (Eq. (5)); hydroxyl radicals generated from two

routes, i. e., the reaction of holes with H_2O (Eq. (6)) and the reaction of superoxide radicals with H^+ and electrons (Eq. (7)). To determine the specific oxidization pathway of PNP in the presence of SR–6 h, ESR (electron spin resonance) spin-trap technique (with DMPO) was employed to monitor the reactive oxygen species generated. As shown in Fig. 6A, both signals of DMPO-$•OH$ and DMPO-$O_2^{•-}$ could be clearly observed when SR–6 h suspension was irradiated by the UV light, which explains both hydroxyl radicals and $O_2^{•-}$ radicals oxidation might be involved in the photocatalysis process. Further, in the controlled photocatalytic experiments (Fig. 6B), a hole scavenger (methanol), an oxygen removal agent (pure N_2), and a hydroxyl radical scavenger (t-butanol) were dropped into or bubbled through the PNP solutions. The addition of methanol or N_2 clearly decreased the degradation efficiency of PNP but the degradation still occurred, while the addition of t-butanol almost completely prevented the PNP degradation. Taking into account the generation of hydroxyl radicals has two routes (Eqs. (6) and (7)), holes or superoxide radicals could not directly oxidize PNP; the PNP degradation follows a hydroxyl radical oxidization pathway. Holes and superoxide radicals must be converted to hydroxyl radicals for PNP degradation. The number of hydroxyl radicals generated per unit time would obviously give essential effect on the degradation rate of PNP, which is usually decided by the SSA for a catalyst with a fixed chemical composition. However, for the SnO_2-rGO composites, the loaded amount of SnO_2 on the rGO sheets and the reduction degree of rGO varied with fabrication time. The SSA would not be the only factor influencing the PNP degradation; for example, SR–6 h had a slightly lower SSA but had much higher
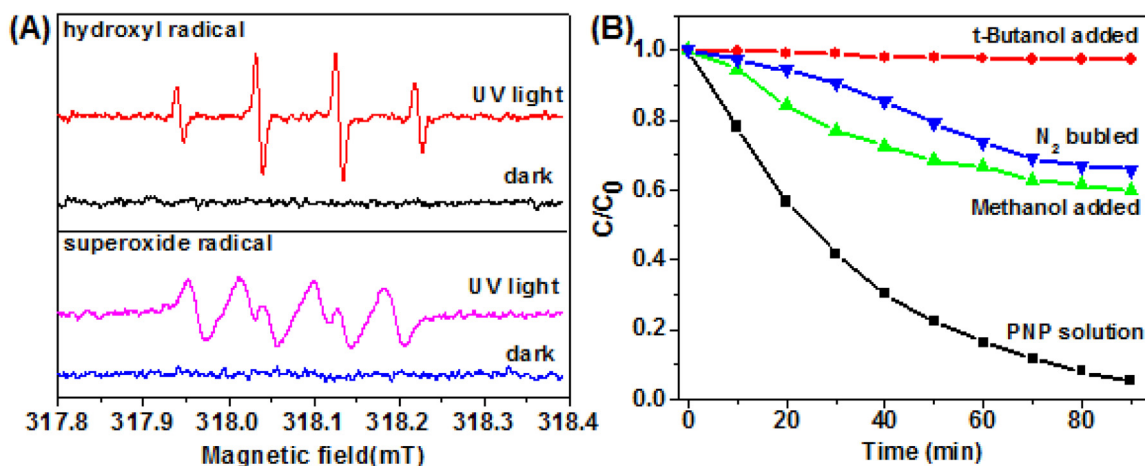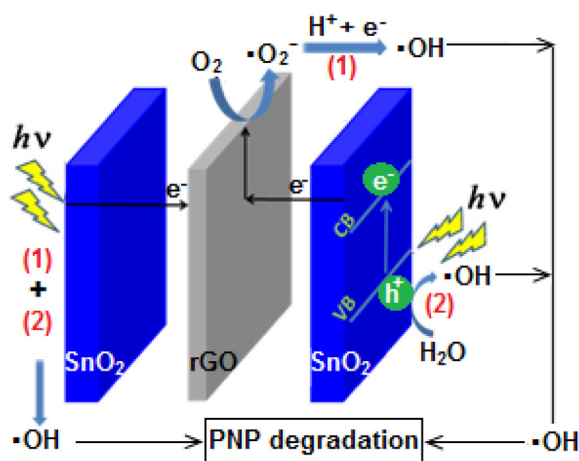
Fig. 6. (A) DMPO spin-trapping ESR spectra of SR–6 h and (B) Photodegradation dynamics of PNP in the presence of SR–6 h with and without addition of *t*-butanol, methanol, or N_2.

activity than SR–3 h. The rGO has an essential role in promoting the generation of hydroxyl radicals.

$$e^- + O_2 \rightarrow {}^\bullet O_2^- \tag{5}$$

$$h^+ + H_2O \rightarrow {}^\circ OH + H^+ \tag{6}$$

$${}^\bullet O_2^- + 2H^+ + 2e^- \rightarrow {}^\circ OH + OH^- \tag{7}$$

Following the above discussion, the proposed mechanism of PNP degradation by the SnO_2-rGO flat composite flake is shown in Scheme 2. By UV irradiation, valence electrons of SnO_2 were excited to the conduction band (Eq. (3)). The SnO_2 layers had been closely contacted with rGO sheets via van der Waals force and electron transfer could occur between them [52]. The work function of chemically reduced GO sheet is around $4.7 \sim 4.8$ eV [53], while that of SnO_2 is about 4.3 eV [54]. Thereby, the rGO here could act as an electron trap and photogenerated electrons could be transferred to the rGO through the SnO_2 layer [55]. The trapped electrons on rGO could react with the dissolved oxygen to generate ${}^\bullet O_2^-$ and ${}^\bullet OH$ following Path (1) [56,57]. Thus, electron-hole recombination rate decreases. Notably, the generation of $\cdot OH$ would focus on the edge of rGO because most of its surface had been covered by the SnO_2 dense layers. The rGO with higher reduction degree had higher conduction and would be more efficient in transferring electrons, preventing electron-hole recombination and promoting the generation of hydroxyl radicals. Holes on the valence band of

SnO_2 directly reacted with absorbed water or hydroxyl groups to form surface $\cdot OH$ (Path (2)). The two SnO_2 layer is equivalent to the generation of hydroxyl radicals. All hydroxyl radicals from the two paths would oxidize PNP molecules.

Based on this mechanism, the varied activities (as shown in Fig. 5A) of SnO_2-based samples could be explained. The pure SnO_2 had the lowest SSA and had a very low activity because of the absence of rGO to separate electron-hole. The low activity of the SR-0.5 h sample could be attributed to the small number of loaded SnO_2 particles, and only a small number of electrons and holes could be generated. The SR–3 h sample had the highest SSA value ($110.8\,m^2/g$) and had an improved activity because SnO_2 porous layers had been formed, providing a larger amount of electrons and holes. However, some SnO_2 layers had been exfoliated (Fig. 3B), and thus, lost the assistance of rGO for electron-hole separation. In addition, the electrons were difficult to be trapped by rGO and the number of the hydroxyl radicals generated from Path (1) was limited because of the low reduction degree of rGO. Hence, the activity was still low. Obviously, a composite with high activity was difficult to obtain at a very short fabrication time. On the contrary, a prolonged fabrication time was also unfavorable, i.e., SR–12 h and SR–24 h samples. Although the reduction degree of rGO could be considerably increased, the samples still had low activities because of the large decrease in the SSA values. Moreover, the incorporated rGO sheets would nearly completely buried and have less chance to come in contact with the dissolved O_2 with increasing densification degree of SnO_2 layers and aggregation of flakes. The hydroxyl radicals from Path (1) would be decreased. At a later fabrication time, the rGO would have less or no effect on the activity of the obtained composite; for example, SR–12 h and SR–24 h actually had very near activity. Different from those composites, the SR–6 h sample had a reasonable structure and was exposed to UV irradiation at a suitable time during the fabrication process. Therefore, this sample had a relatively high SSA value ($106.4\,m^2/g$) and all SnO_2 layers were supported by the rGO sheets with relatively high reduction degree edges, indicating that abundant photogenerated electrons and holes could be produced and the electrons were easily trapped by rGO to improve the electron-hole separation efficiency. Generation of hydroxyl radicals by Path (1) and Path (2) were enhanced and a highly improved activity was obtained.

3.5. Practicality as a photocatalyst

In addition to high activity, stability is essential for practical application of a photocatalyst. However, limited by the fabrication methods, for most graphene-based composites reported previ-
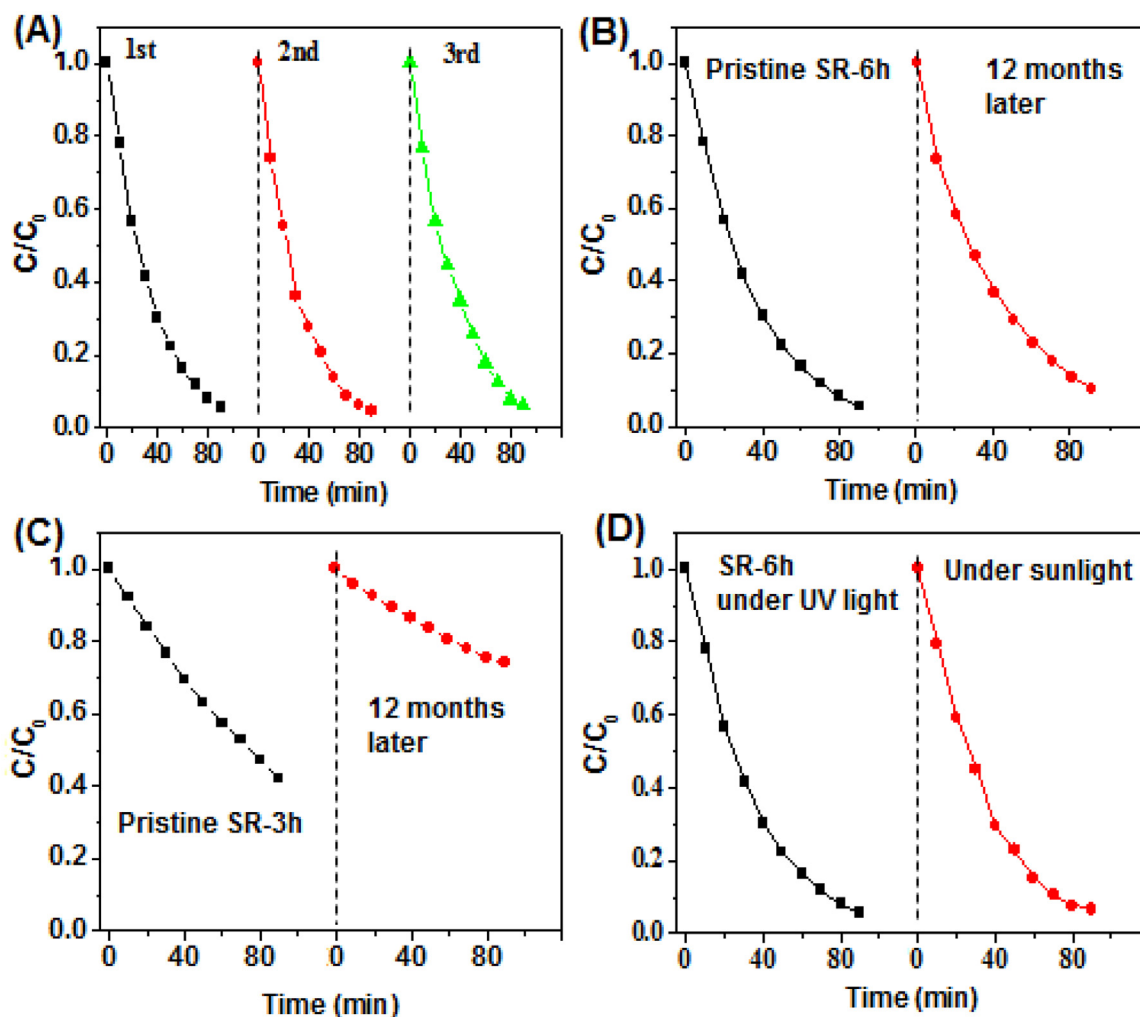

Scheme 2. Schematic of proposed mechanism of PNP degradation in the presence of the flat SnO_2-rGO flake. (1) and (2) respectively represent the two paths to generate hydroxyl radicals.

Fig. 7. Analyses on the stability and the solar photocatalytic activity of SR–6 h. (A) Recyclability of SR–6 h in degradation of PNP; (B) Degradation of PNP by SR–6 h before and after preserved 12 months; (C) Degradation of PNP by SR–3 h before and after preserved 12 months; (D) Degradation of PNP by SR–6 h under UV light and sunlight.

ously, a large proportion of the graphene surface was exposed and the surface easily adsorbed molecules from the environment, which change the property of graphene when they were used or preserved, damaging or even seriously damaging their stability. In this study, the SnO_2 dense layer of the SR–6 h sample could well cover the surface of rGO and block the contact between rGO and the outside molecules. Therefore, the SR–6 h sample had higher stability, which is reflected by its nearly constant photocatalytic activity after recycling three times (Fig. 7A) or preserving exposed to air for more than 12 months (Fig. 7B). By contrast, the SR–3 h sample with partially exposed rGO surfaces showed an obviously decreased activity after preservation at the same time (Fig. 7C); the activity was decreased approximately 67%. Finally, it should be mentioned that the 254-nm low-power (8 W) UV light source chosen in this study had a light intensity of 0.86 mW/cm², which was near to that (0.81–1.26 mW/cm²) of the UV light with the same wavelength in sunlight. Therefore, the SnO_2-rGO composites could be also used in solar photocatalysis. As shown in Fig. 7D, the degradation efficiency of PNP under sunlight was similar to that under UV light in the presence of SR–6 h sample.

4. Conclusion

SnO_2 dense layers on rGO sheets were fabricated by UV irradiation of a mixed aqueous solution of GO, $SnSO_4$, and H_2SO_4. The irradiation time was essential and 6 h of irradiation was optimal

for obtaining the dense layers and the composite unit with a flat flake-like structure composed of two dense layers and an rGO sheet sandwiched in between. During the formation of the dense layers, the GO was gradually reduced by electrons generated from the UV excitation of SnO_2. The dense layers had high mechanical strength and were constituted with closely packed, chemically bonded SnO_2 nanoparticles. Moreover, the dense layers and the rGO sheet had high adhesions, effectively suppressing the flexibility of rGO sheets and immobilizing the flat structure of the composite unit. Such SnO_2-rGO composite was used in the photocatalytic degradation of PNP under low intensity UV light. Hydroxyl radicals were the only oxidants to oxidize the PNP. In addition to having high specific surface area, dense layers were beneficial for the generation of photogenerated carriers. Furthermore, the large area contacts between the dense layer and the rGO sheet was beneficial for the separation of electron-hole, which promoted the generation of hydroxyls and highly improved the activity of the composite. Moreover, the dense layer could block the contact of rGO surface with the outside molecules and increase the long-term stability of the composite. Under sunlight, the composite exhibited similar performances. The construction of dense layers on rGO sheet obviously provides a new way to obtain stable practical graphene-based composites with high performances. In addition to photocatalysis applications, such composite might also be used in sensors, lithium-ion batteries, super capacitors, and solar cells.

Acknowledgments

This work was co-supported by the National Natural Science Foundation of China (No. 21571068), the Research Project of Chinese Ministry of Education (No. 213029A), the Natural Science Foundation of Guangdong Province (No. 2015A030313387), the Science and Technology Program of Guangzhou (No. 201607010301) and the Special funds for Discipline Construction in Guangdong Province (No. 2013KJCX0057).

Appendix A. Supplementary data

Supplementary data associated with this article can be found, in the online version, at http://dx.doi.org/10.1016/j.apcatb.2017.03.082.

References

[1] S.R. Wang, J.D. Yang, H.X. Zhang, Y.S. Wang, X.L. Gao, L.W. Wang, Z.Y. Zhu, Sensor. Actuat. B-Chem. 207 (2015) 83–89.
[2] J. Jońca, A. Ryzhikov, M.L. Kahn, K. Fajerwerg, A. Chapelle, P. Menini, P. Fau, Chem. Eur. J. 22 (2016) 10127–10135.
[3] J.H. Um, M. Choi, H. Park, Y.H. Cho, D.C. Dunand, H. Choe, Y.E. Sung, Sci. Rep. 6 (2016) 18626.
[4] N. Srivastava, M. Mukhopadhyay, Ind. Eng. Chem. Res. 53 (2014) 13971–13979.
[5] R. Manjula, ACS Appl. Mater. Interfaces 4 (2012) 6252–6260.
[6] A.K. Sinha, M. Pradhan, S. Sarkar, T. Pal, Environ. Sci. Technol. 47 (2013) 2339–2345.
[7] S.W. Liu, G.C. Huang, J.G. Yu, T.W. Ng, H.Y. Yip, P.K. Wong, ACS Appl. Mater. Interfaces 6 (2014) 2407–2414.
[8] P. Li, Y. Lan, Q. Zhang, Z.Y. Zhao, T. Pullerits, K.B. Zheng, Y. Zhou, J. Phys. Chem. C 120 (2016) 9253–9262.
[9] M.T. Uddi, Y. Nicolas, C. Olivier, T. Toupance, L. Servant, M.M. Müller, H.J. Kleebe, J. Ziegler, W. Jaegermann, Inorg. Chem. 51 (2012) 7764–7773.
[10] M.T. Niu, F. Huang, L.F. Cui, P. Huang, Y.L. Yu, Y.S. Wang, ACS Nano 4 (2010) 681–688.
[11] Z.Y. Liu, D.L. Sun, P. Guo, J.O. Leckie, Nano Lett. 7 (2007) 1081–1085.
[12] A. Tanaka, K. Hashimoto, H. Kominami, Chem. Eur. J. 22 (2016) 4592–4599.
[13] M.M. Khan, S.A. Ansari, M.E. Khan, M.O. Ansari, B.K. Min, M.H. Cho, New J. Chem. 39 (2015) 2758–2766.
[14] A.M. Al-Hamdi, M. Sillanpää, J. Dutta, J. Alloy. Compd. 618 (2015) 366–371.
[15] V. Kumar, A. Govind, R. Nagarajan, Inorg. Chem. 50 (2011) 5637–5645.
[16] L.C. Chen, L.Z. Xie, M.Z. Wang, X.W. Ge, J. Mater. Chem. A 3 (2015) 2991–2998.
[17] X.Y. Pan, Z.G. Yi, ACS Appl. Mater. Interfaces 7 (2015) 27167–27175.
[18] J. Wei, S.L. Xue, P. Xie, R.J. Zou, Appl. Surf. Sci. 376 (2016) 172–179.
[19] K.S. Novoselov, A.K. Geim, S.V. Morozov, D. Jiang, Y. Zhang, S.V. Dubonos, I.V. Grigorieva, A.A. Firsov, Science 306 (2004) 666–669.
[20] M.J. Allen, V.C. Tung, R.B. Kaner, Chem. Rev. 110 (2010) 132–145.
[21] D. Mateo, I. Esteve-Adel, J. Albero, J.F.S. Royo, A. Primo, H. Garcia, Nat. Commun. 7 (2016) 11819.
[22] S.Q. Song, B. Cheng, N.S. Wu, A.Y. Meng, S.W. Cao, J.G. Yu, Appl. Catal. B-Environ. 181 (2016) 71–78.
[23] F. Perreault, A.F. de Faria, M. Elimelech, Chem. Soc. Rev. 44 (2015) 5861–5896.
[24] Y.Y. Fan, W.G. Ma, D.X. Han, S.Y. Gan, X.D. Dong, L. Niu, Adv. Mater. 27 (2015) 3767–3773.
[25] H. Seema, K.C. Kemp, V. Chandra, K.S. Kim, Nanotechnology 23 (2012) 355705.
[26] S.D. Zhuang, X.Y. Xu, B. Feng, J.G. Hu, Y.R. Pang, G. Zhou, L. Tong, Y.X. Zhou, ACS Appl. Mater. Interfaces 6 (2014) 613–621.
[27] Y.L. Cao, Y.Z. Li, D.Z. Jia, J. Xie, RSC Adv. 4 (2014) 46179–46186.
[28] E. Lee, J.Y. Hong, H. Kang, J. Jang, J. Hazard. Mater. 219–220 (2012) 13–18.
[29] P. Gao, Z.Y. Liu, M.H. Tai, D.D. Sun, W. Ng, Appl. Catal. B-Environ. 138 (2013) 17–25.
[30] M.Z. Ge, S.H. Li, J.Y. Huang, K.Q. Zhang, S.S. Al-Deyab, Y.K. Lai, J. Mater. Chem. A 3 (2015) 3491–3499.
[31] L.C. Chen, L.Z. Xie, M.Z. Wang, X.W. Ge, J. Mater. Chem. A 3 (2015) 2991–2998.
[32] W. Zhai, F.Q. Sun, W. Chen, Z.Z. Pan, L.H. Zhang, S.H. Li, S.L. Feng, Y.Y. Liao, W.S. Li, Appl. Catal. A- Gen. 454 (2013) 59–65.
[33] D. Méndez, R. Vargas, C. Borrás, S. Blanco, J. Mostany, B.R. Scharifker, Appl. Catal. B-Environ. 166–167 (2015) 529–534.
[34] W.S. Hummers, R.E. Offema, J. Am. Chem. Soc. 80 (1958) 1339.
[35] C. Chen, W.M. Cai, M.C. Long, B.X. Zhou, Y.H. Wu, D.Y. Wu, Y.J. Feng, ACS Nano 4 (2010) 6425–6432.
[36] P.A. Russo, N. Donato, S.G. Leonardi, S. Baek, D.E. Conte, G. Neri, N. Pinna, Angew. Chem. Int. Ed. 51 (2012) 11053–11057.
[37] M.S.A.S. Shah, A.R. Park, K. Zhang, J.H. Park, P.J. Yoo, ACS Appl. Mater. Interfaces 4 (2012) 3893–3901.
[38] H. Bai, Y.X. Xu, L. Zhao, C. Li, G.Q. Shi, Chem. Commun. 13 (2009) 1667–1669.
[39] D.X. Yang, A. Velamakanni, G. Bozoklu, S. Park, M. Stoller, R.D. Piner, S. Stankovich, I. Jung, D.A. Field, C.A. Ventrice, R.S. Ruoff, Carbon 47 (2009) 145–152.
[40] G.M. An, N. Na, X.R. Zhang, Z.J. Miao, S.D. Miao, K.L. Ding, Z.M. Liu, Nanotechnology 18 (2007) 435707.
[41] A. Diéguez, A. Romano-Rodríguez, A. Vilà, J.R. Morante, J. Appl. Phys. 90 (2001) 1550–1557.
[42] A. Ayeshamariam, S. Ramalingam, M. Bououdina, M. Jayachandran, Spectroc. Acta Pt. A-Molec. 118 (2014) 1135–1143.
[43] S. Stankovich, D.A. Dikin, R.D. Piner, K.A. Kohlhaas, A. Kleinhammes, Y.Y. Jia, Y. Wu, S.T. Nguyen, R.S. Ruoff, Carbon 45 (2007) 1558–1565.
[44] K. Vinodgopal, B. Neppolian, I.V. Lightcap, F. Grieser, M. Ashokkumar, P.V. Kamat, J. Phys. Chem. Lett. 1 (2010) 1987–1993.
[45] M. Zhang, D.N. Lei, Z.F. Du, X.M. Yin, L.B. Chen, Q.H. Li, Y.G. Wang, T.H. Wang, J. Mater. Chem. 21 (2011) 1673–1676.
[46] B. Tang, G.X. Hu, H.Y. Gao, Appl. Spectrosc. Rev. 45 (2010) 369–407.
[47] S.Y. Li, T. Qian, S.S. Wu, J. Shen, Chem. Commun. 48 (2012) 7997–7999.
[48] M. Ichimura, K. Shibayama, K. Masui, Thin Solid Films 466 (2004) 34–36.
[49] S.P. Xu, F.Q. Sun, F.L. Gu, Y.B. Zuo, L.H. Zhang, C.F. Fan, S.M. Yang, W.S. Li, ACS Appl. Mater. Interfaces 6 (2014) 1251–1257.
[50] O. Akhavan, M. Abdolahad, A. Esfandiar, M. Mohatashamifar, J. Phys. Chem. C 114 (2010) 12955–12959.
[51] W. Chen, F.Q. Sun, Z.M. Zhu, Z.L. Min, W.S. Li, Microporous Mesoporous Mat. 186 (2014) 65–72.
[52] B. Bukowski, N.R. Deskins, Phys. Chem. Chem. Phys. 17 (2015) 29734–29746.
[53] S.T. Han, Y. Zhou, C.D. Wang, L.F. He, W.J. Zhang, V.A.L. Roy, Adv. Mater. 25 (2013) 872–877.
[54] L.J. Wang, J.Y. Lin, Y. Ye, T.L. Guo, J. Phys. Status Solidi C 9 (2012) 52–54.
[55] P.V. Kamat, J. Phys. Chem. Lett. 2 (2011) 242–251.
[56] H.T. Chen, X.M. Pu, M. Gu, J. Zhu, L.W. Cheng, Ceram. Int. 42 (2016) 17717–17722.
[57] L.C. Chen, L.Z. Xie, M.Z. Wang, X.W. Ge, J. Mater. Chem. A 3 (2015) 2991–2998.